

ARTICLE

Open Access

# Nanomorphology dependence of the environmental stability of organic solar cells

Woong Sung<sup>1</sup>, Hansol Lee<sup>1,2</sup>, Wookjin Choi<sup>1</sup>, Se Gyo Han<sup>1</sup>, Jimin Kim<sup>1</sup>, Kwangwoo Cho<sup>1</sup>, Seung Hyun Kim<sup>1</sup>, Dongki Lee<sup>3</sup>, Hyung Do Kim<sup>4</sup>, Hideo Ohkita<sup>4</sup> and Kilwon Cho<sup>1</sup>

## Abstract

Previous studies have reported contradictory effects of small-molecule acceptors on the environmental stability of polymer:small-molecule blends, with one showing that a small-molecule acceptor stabilizes and another showing that it destabilizes the polymer donor. In this work, to investigate the origin of these contradictory results, the effects of the nanomorphologies of small-molecule acceptors on the environmental stability of polymer:small-molecule blends are demonstrated. Investigations on the environmental stabilities of polymer:fullerene blends of poly[[4,8-bis[(2-ethylhexyl)oxy]benzo[1,2-*b*:4,5-*b'*]dithiophene-2,6-diyl][3-fluoro-2-[(2-ethylhexyl)carbonyl]thieno[3,4-*b*]thiophenediyl]] (PTB7):phenyl-C<sub>61</sub>-butyric acid methyl ester (PCBM) with contrasting nanomorphologies of PCBM reveal that dispersed PCBM in a mixed phase is the critical factor that causes triplet-mediated singlet oxygen generation and, hence, the severe photooxidation of PTB7, whereas an aggregated PCBM phase stabilizes PTB7 by reducing the formation of PTB7 triplet excitons. In addition, the photooxidation of PTB7 substantially degrades hole transport in the PTB7:PCBM blends by destroying the crystalline PTB7 phases within the films; this effect is strongly correlated with the efficiency losses of the PTB7:PCBM organic solar cells. These conclusions are also extended to polymer:nonfullerene blends of PTB7:ITIC and PTB7:Y6, thereby confirming the generality of this phenomenon for polymer:small-molecule organic solar cells.

## Introduction

Long-standing research efforts have been made to discover conjugated polymer donors and small-molecule acceptors with excellent optical and electrical properties and have bolstered the field of organic solar cells (OSCs), resulting in an increase in device efficiencies from 3 to >18% in the past decade<sup>1,2</sup>. These excellent device efficiencies originate from the complex morphologies of polymer:small-molecule bulk heterojunction (BHJ) blends, which consist of a mixed phase and pure crystalline or amorphous phase of both donor and acceptor<sup>3–8</sup>. A mixed phase achieves ultrafast charge separation after

photoexcitation, whereas a pure phase achieves efficient transport of separated charges to the electrode<sup>4,9</sup>. However, a weakly crystalline phase facilitates the fast diffusion of extrinsic species, such as molecular oxygen and water, making OSC devices prone to degradation<sup>10,11</sup>. In particular, exposure to light and molecular oxygen has been identified as a primary origin of degradation as a result of triplet-mediated singlet oxygen generation or anion-mediated superoxide generation<sup>10–14</sup>, both of which substantially limit the environmental stability of OSCs. Although device encapsulation can form a physical barrier against the diffusion of molecular oxygen into a device<sup>15,16</sup>, encapsulation technology greatly increases fabrication costs, making OSCs far from a low-cost renewable energy source. Identifying the exact degradation mechanism of OSC devices and improving their intrinsic stability are therefore critical steps toward their commercialization.

Correspondence: Hyung Do Kim (hyungdokim@photo.polym.kyoto-u.ac.jp) or Kilwon Cho (kwcho@postech.ac.kr)

<sup>1</sup>Department of Chemical Engineering, Pohang University of Science and Technology (POSTECH), Pohang 37673, Republic of Korea

<sup>2</sup>Department of Chemical and Biological Engineering, Gachon University, Seongnam 13120, Republic of Korea

Full list of author information is available at the end of the article

These authors contributed equally: Woong Sung, Hansol Lee.

© The Author(s) 2022



**Open Access** This article is licensed under a Creative Commons Attribution 4.0 International License, which permits use, sharing, adaptation, distribution and reproduction in any medium or format, as long as you give appropriate credit to the original author(s) and the source, provide a link to the Creative Commons license, and indicate if changes were made. The images or other third party material in this article are included in the article's Creative Commons license, unless indicated otherwise in a credit line to the material. If material is not included in the article's Creative Commons license and your intended use is not permitted by statutory regulation or exceeds the permitted use, you will need to obtain permission directly from the copyright holder. To view a copy of this license, visit <http://creativecommons.org/licenses/by/4.0/>.

Most previous related studies have found that pristine films of amorphous organic semiconductor materials are more vulnerable to degradation than their crystalline counterparts. Compared with films composed of crystalline materials, films composed of amorphous materials include a higher volume fraction of amorphous phase<sup>10,11</sup>. This high volume of amorphous phase increases the diffusion of extrinsic species through the films. In addition, amorphous materials exhibit poor planarity of their conjugated backbone compared with their crystalline counterparts and are therefore vulnerable to photoinduced conformational changes, followed by rapid photooxidation<sup>17,18</sup>. For polymer:small-molecule blends, however, their environmental stability is difficult to predict because it changes without a distinct trend as the combination of polymer and small-molecule changes<sup>19,20</sup>. For example, fullerenes, such as phenyl-C<sub>61</sub>-butyric acid methyl ester (PCBM), have been shown to stabilize numerous polymer donors under illumination in ambient air by quenching singlet excitons and scavenging radicals<sup>21–23</sup>. However, these results contradict some previous studies that have shown that PCBM accelerates the photooxidation of polymer donors by increasing triplet-mediated singlet oxygen generation<sup>19,20,24</sup>. The reasons for these different stabilization/destabilization effects of PCBM remain unclear. This lack of clarity is partly attributable to previous studies that typically addressed dissimilar material systems that contained different volume fractions of dispersed and aggregated PCBM phases, considering that a previous study reported that the change in the photooxidative stability of pristine PCBM depends on the nanomorphology of PCBM<sup>25</sup>. Although this previous study was limited to the environmental stability of pristine PCBM, we expect that the degree of fullerene aggregation could also cause different stabilization/destabilization pathways in conjugated polymer:fullerene blends. That is, the relative volume fractions of the dispersed phase and aggregated phase might strongly influence the environmental stability of OSC devices.

The exact mechanism by which oxidized conjugated polymer donors degrade OSC devices is also poorly understood. Polymer donors undergo a change in chemical structure upon photooxidation, such as the cleavage of their side chains or oxidation of their backbone; such changes typically lead to a loss of extended  $\pi$ -conjugation in the polymer donors<sup>26–29</sup>. This loss of conjugation is accompanied by a broadening of the bandgap; thus, most studies on oxidized donor polymers have highlighted the loss of light absorption in describing the efficiency loss in OSC devices<sup>10–14</sup>. However, the loss of efficiency is generally much larger than the loss of light absorption, with a weak correlation observed between them. That is, the diminished electrical properties caused by oxidized donor polymers could further contribute to efficiency loss in

OSC devices, considering that a previous study has reported that the photooxidation of donor polymers accompanies morphological degradation<sup>30</sup>.

Herein, we systematically investigate the influence of the nanomorphology of a small-molecule acceptor on the environmental stability of OSC devices based on polymer:small-molecule blends. We address this issue in a system composed of poly[[4,8-bis[(2-ethylhexyl)oxy]benzo[1,2-*b*:4,5-*b'*]dithiophene-2,6-diyl][3-fluoro-2-[(2-ethylhexyl)carbonyl]thieno[3,4-*b*]thiophenediyl]] (PTB7) and PCBM. Although OSC devices based on PCBM exhibit lower efficiencies than those based on nonfullerene acceptors<sup>1,2</sup>, the highly miscible nature of PCBM is an advantage in controlling the nanomorphology of PCBM in blends<sup>25,31</sup>. By varying the weight ratio (wt%) of PCBM, we prepared (1) a pristine PTB7, (2) an 80:20% PTB7:PCBM blend, which mainly contains dispersed PCBM, and (3) a 50:50% PTB7:PCBM blend, which contains not only dispersed PCBM but also aggregated PCBM due to the increased weight fraction of PCBM. These three films were subjected to aging under simulated AM 1.5 G illumination in dry air (20–30% RH), and their environmental stabilities were compared. This enabled us to distinguish the effects of dispersed PCBM and aggregated PCBM on the environmental stabilities of PTB7:PCBM blends. Surprisingly, we found that the environmental instabilities of the PTB7:PCBM blends stemmed from the dispersed PCBM in the mixed phase, which led to the severe photooxidation of PTB7 after only a few minutes of illumination in dry air. We showed that dispersed PCBM accelerated the formation of PTB7 triplet excitons by bimolecular recombination, leading to the generation of singlet oxygen, followed by the photooxidation of PTB7. However, the aggregated PCBM phase suppressed the photooxidation of PTB7 by alleviating the formation of PTB7 triplet excitons. In addition, the accelerated photooxidation of PTB7 in the PTB7:PCBM blend enabled us to investigate the influence of oxidized PTB7 on the efficiency of PTB7:PCBM OSC devices. We found that oxidized PTB7 substantially degrades hole transport in the films by decreasing the fraction of the crystalline PTB7 phase, thereby decreasing the number of hole transport pathways within the films. In particular, hole transport in the PTB7:PCBM blends degrades much faster than light absorption, which shows a strong correlation to the efficiency loss in OSC devices. These results signify the importance of controlling the nanomorphologies of small-molecule acceptors to achieve high environmental stability of polymer:small-molecule blends. We further extend our conclusions to other blend systems composed of other benchmark nonfullerene acceptors, suggesting that the degradation pathways presented herein are applicable to other high-performance polymer:nonfullerene OSC devices.

## Materials and methods

### Materials

All chemicals and reagents were purchased from commercial sources and used as received without any further purification. Chlorobenzene (CB) anhydrous (99.8%) was purchased from Sigma–Aldrich. PTB7 was purchased from Solarmer Energy Inc. PCBM was purchased from Solenne BV. 3,9-bis(2-methylene-(3-(1,1-dicyanomethylene)-indanone))-5,5,11,11-tetrakis(4-hexylphenyl)-dithieno[2,3-d:2',3'-d']-s-indaceno[1,2-b:5,6-b']-dithiophene (ITIC) and 2,2'-((2Z,2'Z)-((12,13-bis(2-ethylhexyl)-3,9-diundecyl-12,13-dihydro-[1,2,5]thiadiazolo[3,4-e]thieno[2'',3''':4',5']thieno[2',3':4,5]pyrrolo[3,2-g]thieno[2',3':4,5]thieno[3,2-b]indole-2,10-diy))bis(methanylylidene))bis(5,6-difluoro-3-oxo-2,3-dihydro-1*H*-indene-2,1-diylidene))dimalononitrile (Y6) were purchased from Derthon Optoelectronic Materials Science Technology Co Ltd. Poly(3,4-ethylenedioxythiophene) polystyrene sulfonate (PEDOT:PSS) water dispersion (Clevios VP AL 4083) was purchased from Heraeus.

### Fabrication of fresh and aged OSC devices

OSC devices were fabricated with conventional structures of ITO/PEDOT:PSS/PTB7:PCBM/LiF/Al and with inverted structures of ITO/zinc oxide (ZnO)/PTB7:PCBM/MoO<sub>3</sub>/Al. Prepatterned ITO-coated glass substrates were cleaned by performing sequential sonications in soapy water, deionized (DI) water, acetone, and 2-propanol for 20 min each. The cleaned substrates were further treated with UV-ozone for 15 min to increase the wettability. For the bottom electrodes of the conventional OSC devices, PEDOT:PSS solution was spin-coated on the ITO-coated glass at 4000 rpm for 60 s and then annealed in ambient air at 120 °C for 30 min. For the bottom electrodes of the inverted OSC devices, a ZnO precursor solution was prepared by dissolving zinc acetate dihydrate (C<sub>4</sub>H<sub>6</sub>O<sub>4</sub>Zn·2(H<sub>2</sub>O), 99.5%, Sigma–Aldrich, 1 g) and monoethanolamine (HOCH<sub>2</sub>CH<sub>2</sub>NH<sub>2</sub>, 98%, Acros, 0.252 g) in 2-methoxyethanol (10 mL) with stirring for 8 h to achieve hydrolysis and aging. The ZnO precursor solution was spin-coated on ITO-coated glass at 5000 rpm for 60 s and then annealed in ambient air at 180 °C for 1 h. PTB7 and PCBM were dissolved in CB with a weight ratio of 50:50 wt% and a donor concentration of 10 mg mL<sup>-1</sup> and then stirred at 55 °C for 12 h in a nitrogen-filled glovebox. The PTB7:PCBM blend solution was spin-coated on ITO/PEDOT:PSS substrates or ITO/ZnO substrates at 1500 rpm for 60 s in a nitrogen-filled glovebox. ITO/PEDOT:PSS/PTB7:PCBM and ITO/ZnO/PTB7:PCBM were exposed to stimulated AM 1.5 G illumination in dry air for different aging times (0–120 min). Finally, a 6 Å LiF layer followed by a 100 nm Al layer for the top electrodes of conventional OSC devices and a

10 nm MoO<sub>3</sub> layer followed by a 100 nm Al layer for the top electrodes of inverted OSC devices were deposited using thermal evaporation at a pressure of less than  $4 \times 10^{-6}$  Torr.

### Fabrication of fresh and aged hole-only devices

Hole-only devices were fabricated with structures of ITO/PEDOT:PSS/PTB7:PCBM/MoO<sub>3</sub>/Al. The ITO/PEDOT:PSS bottom electrodes were prepared similar to those used in the OSC devices. PTB7 and PCBM were dissolved in CB at wt% ratios of 100:0, 80:20, and 50:50 and then stirred at 55 °C for 12 h in a nitrogen-filled glovebox. To minimize variations in the volume and morphology of PTB7 in each PTB7:PCBM blend with different fractions of PCBM, all PTB7:PCBM blends were prepared from a pristine CB solution with a fixed concentration of PTB7 by spin-coating at a constant velocity of 1500 rpm. Pristine PTB7 films and PTB7:PCBM blend films were exposed to simulated AM 1.5 G illumination in dry air for different aging times (0–120 min). Finally, a 10-nm MoO<sub>3</sub> layer followed by a 100 nm Al layer was deposited as the top electrode using thermal evaporation at a pressure of  $<4 \times 10^{-6}$  Torr.

### Characterization of OSC devices and hole-only devices

Current–voltage (*J–V*) characteristics were recorded using a solar simulator (Newport, Oriel Class A) and a source meter (Keithley 4200) in a nitrogen-filled glove box. The illumination was set to AM 1.5 G and calibrated to 100 mW cm<sup>-2</sup> by using a Reference Cell PVM 132 calibrated at the US National Renewable Energy Laboratory. The external quantum efficiency (EQE) spectra were measured using a photomodulation spectroscopic setup (Merlin, Oriel) with monochromatic light from a Xenon lamp. The device area for the *J–V* measurements and EQE measurements was 0.0555 cm<sup>2</sup>. The dark *J–V* characteristics of the hole-only devices were recorded using a source meter (Keithley 4200) in a nitrogen-filled glove box.

### Characterization of thin films

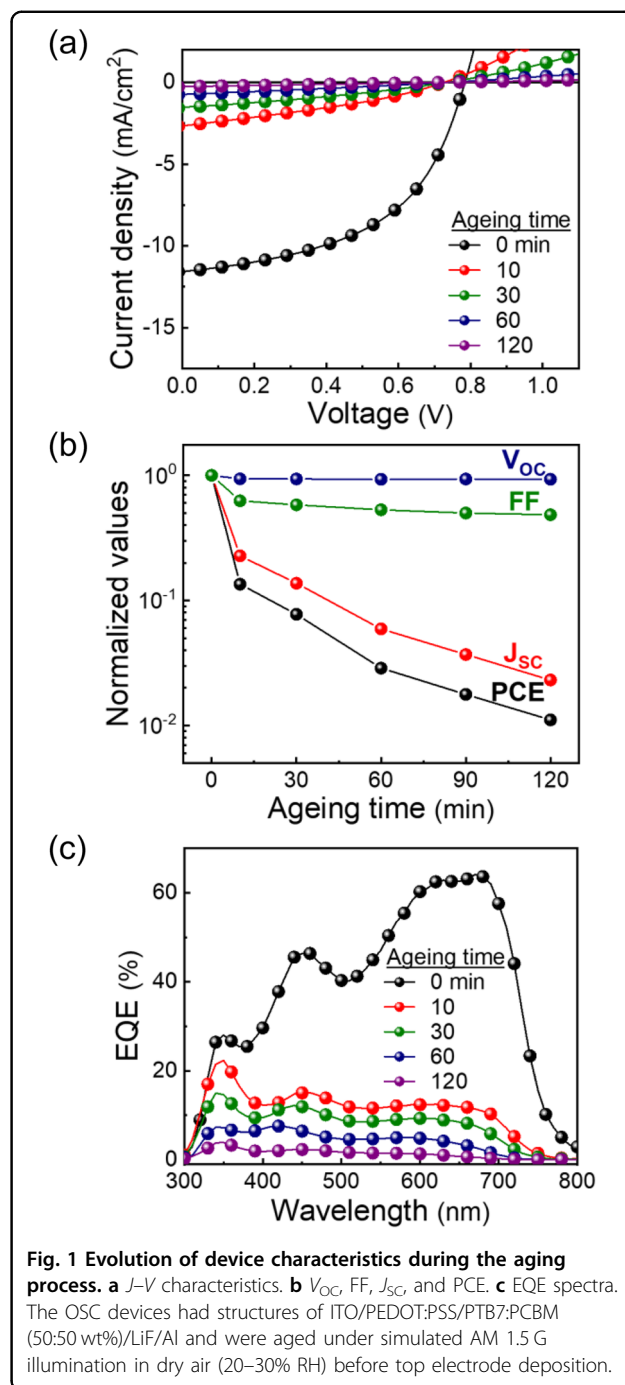
For the measurements of thin films, materials were spin-coated onto substrates under identical solutions to those used to fabricate the OSC devices or hole-only devices. The ultraviolet–visible (UV–Vis) absorption and photoluminescence (PL) spectra of the films coated on glass were recorded using a Varian CARY-5000 UV–Vis spectrophotometer and an FP-6500 spectrofluorometer (Jasco), respectively. Fourier transform infrared (FTIR) spectra of the films coated on Si substrates were recorded using Vertex 70 v (Bruker). Matrix-assisted laser desorption/ionization time-of-flight (MALDI-TOF) spectra were acquired in negative-reflection mode using an Autoflex Speed LRF (Bruker), which was equipped with a Smartbeam-II Nd:YAG laser ( $\lambda = 355$  nm). The samples

for MALDI-TOF measurements were prepared by redissolving the films in CB after photochemical degradation, and *trans*-2-[3-(4-*tert*-butylphenyl)-2-methyl-2-propenylidene]malononitrile (DCTB) was used as the MALDI matrix. Grazing-incidence wide-angle X-ray scattering (GIWAXS) measurements of the films coated on PEDOT:PSS/Si substrates were performed using the synchrotron source at the 5A beamlines of the Pohang Accelerator Laboratory (PAL) in Korea. The photon energy was 10.6408 keV ( $\lambda = 1.1651 \text{ \AA}$ ), and the critical angle was  $\sim 0.12^\circ$ . The atomic force microscopy (AFM) images of the films coated on PEDOT:PSS/Si substrates were characterized using Digital Instruments Multimode 8-HR AFM (Bruker). The thicknesses of the films coated on PEDOT:PSS/ITO/glass substrates were measured using AFM (Digital Instruments Multimode 8-HR AFM, Bruker). Scanning electron microscopy (SEM) images of the films coated on PEDOT:PSS/Si substrates were characterized using Hitachi S-4800. Microsecond transient absorption (TA) spectra of the films coated on quartz were acquired using a highly sensitive microsecond TA system. The samples were excited at a wavelength of 532 nm with a fluence of  $1.7 \mu\text{J cm}^{-2}$  using a Nd:YAG laser (ELforlight, SPOT-10-200-532), providing subnanosecond pulses at a repetition rate of 4 Hz. A tungsten lamp (Thermo-Oriel, Model 66997) with an intensity controller (Thermo-Oriel, Model 66950) was employed as a probe light source. The probe wavelength was selected by two monochromators (Ritsu, MC-10C). To suppress scattered light and emission, an appropriate optical cutoff filter was equipped before and after the sample. The temporal evolution of  $\Delta\text{OD}$  was reduced with a high-gain Si photodiode (Hamamatsu Photonics, S1722-01). The signal from the photodiode was preamplified and then sent to a main amplifier (Costronics Electronics) with an electronic bandpass filter to enhance the signal-to-noise ratio. The resultant amplified signal was collected using a digital oscilloscope (Tektronix, TDS2022), which was synchronized with the trigger signal of a laser pulse from a Si photodiode (Thorlabs Inc., DET10A). TA decays were collected over the time range from 500 ns to  $\mu\text{s}$ , averaging 4000 laser shots on each decay time scale, which yields a sensitivity of  $10^{-6}$  to  $10^{-4}$ . Note that laser irradiation had negligible impacts on sample degradation, at least under these experimental conditions, since the resultant data were highly reproducible even after several measurements.

## Results and discussion

### Photooxidation of PTB7 in PTB7:PCBM OSC devices

We investigated the decrease in efficiency due to the degradation of PTB7:PCBM BHJ OSC devices upon exposure to light and oxygen. Figure 1a shows the evolution of the  $J$ - $V$  characteristics of OSC devices based on



a PTB7:PCBM blend (50:50%) subjected to aging under simulated AM 1.5 G illumination in dry air for various times (see detailed photovoltaic parameters in Table S1). The PTB7:PCBM blends were processed from a pristine CB solution and aged prior to the deposition of the top electrode to rule out the possibility of degradation by the solvent additive or top electrode. The PTB7:PCBM OSC devices exhibited substantial environmental instabilities, showing an efficiency loss of 86% after only 10 min of

aging and 99% after 120 min, as indicated by a simultaneous decrease in the short-circuit current density ( $J_{SC}$ ) and fill factor (FF) (Fig. 1b). These experiments were repeated using an inverted device structure with a ZnO bottom electrode (Fig. S1), which showed  $J$ - $V$  characteristics similar to those of the devices represented in Fig. 1a. Furthermore, the OSC devices aged prior to deposition of the active layer, in which the bottom electrode (PEDOT:PSS) was selectively aged, showed  $J$ - $V$  characteristics similar to those of the fresh OSC devices (Table S2), indicating that the efficiency losses in the OSC devices originated from the degradation of the PTB7:PCBM blends. The OSC devices exposed to dry air in the dark showed  $J$ - $V$  characteristics similar to those of fresh OSC devices (Table S2). Furthermore, the OSC devices exposed to light in dry air exhibit much faster efficiency losses than the OSC devices exposed to light in inert nitrogen. Although degradation in inert nitrogen is known to be caused by demixing<sup>32–35</sup>, accelerated degradation in ambient air confirms that the degradation of the PTB7:PCBM blends in this study was mainly driven by the combination of light and oxygen.

To identify which component in the PTB7:PCBM blends mainly degrades, we conducted EQE and MALDI-TOF mass spectrometry measurements. Figure 1c shows the evolution of the EQE spectra of the PTB7:PCBM OSC devices subjected to aging for different times under illumination in dry air. The overall EQE response gradually decreased with increasing aging time. In particular, the EQE response in the 500–800 nm region, which is

consistent with the absorption profile of PTB7 (Fig. S2), decreased substantially after 120 min of aging, where the highest EQE value decreased from 64% to 1.5%, exhibiting a similar trend as the decrease in  $J_{SC}$  (Table S1). In contrast, only a small amount of oxidized PCBM species was detected in the MALDI-TOF spectrum of the aged PTB7:PCBM blends (Fig. S3), indicating that degradation of PTB7 mainly occurred in PTB7:PCBM blends during aging. Previous studies have indicated that PCBM causes the photooxidation of PTB7<sup>19,20,24</sup>, which accelerates the generation of singlet oxygen in PTB7:PCBM blends.

### Nanomorphology of PCBM and its relation to photooxidation of PTB7 in PTB7:PCBM blends

To understand how PCBM causes the photooxidation of PTB7, we systematically studied the link between the nanomorphology of PCBM and the environmental stabilities of PTB7:PCBM blends. For this purpose, we prepared three PTB7:PCBM blends with different weight ratios of PCBM: (1) pristine PTB7 (100:0 wt%), (2) a blend with a low weight ratio of PCBM (80:20 wt%), and (3) a blend with a high weight ratio of PCBM (50:50 wt%). To characterize the blend morphologies of samples with different weight fractions of PCBM, we used a combination of AFM (Fig. 2a), GIWAXS (Fig. 2b), PL spectroscopy (Fig. S4), and cross-sectional SEM (Fig. S5). Pristine PTB7 exhibited smooth height images, with an estimated root-mean-square roughness ( $r_{RMS}$ ) of 0.67 nm, and showed positive phase images (Fig. 2a, top panel). The GIWAXS patterns showed a (100) reflection at  $0.32 \text{ \AA}^{-1}$  along the

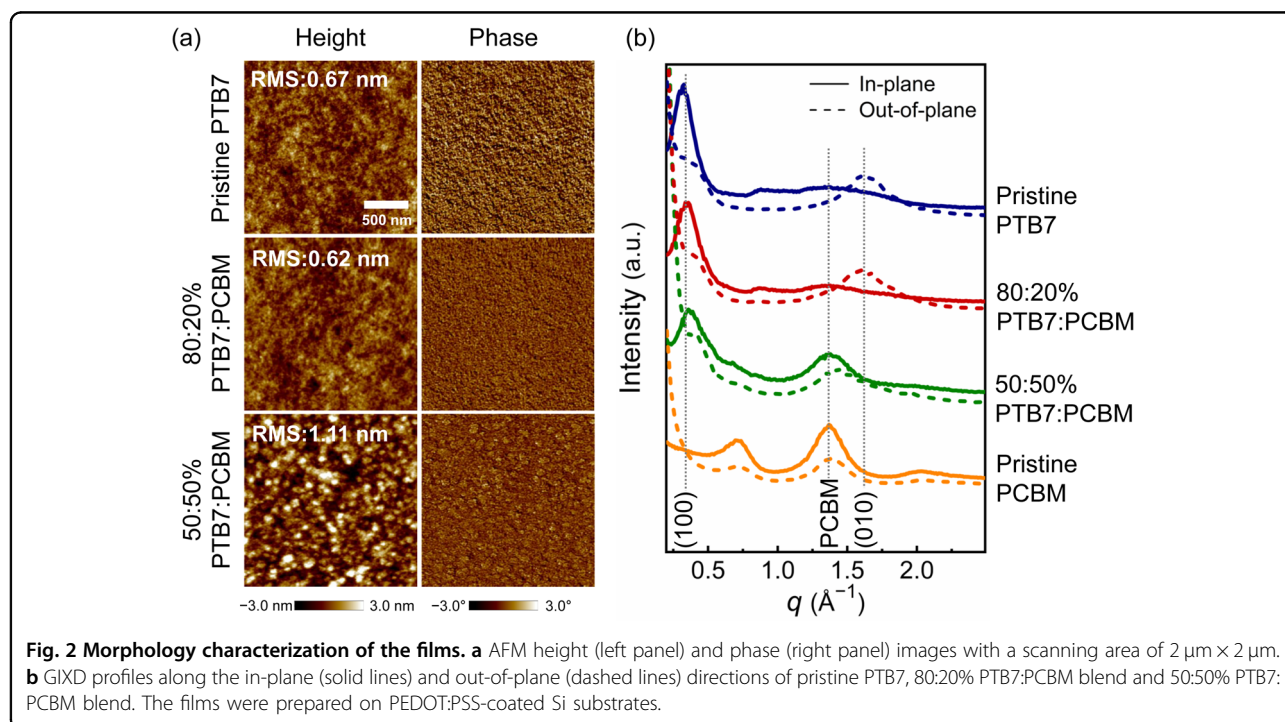


**Fig. 2** Morphology characterization of the films. **a** AFM height (left panel) and phase (right panel) images with a scanning area of  $2 \mu\text{m} \times 2 \mu\text{m}$ . **b** GIWAXS profiles along the in-plane (solid lines) and out-of-plane (dashed lines) directions of pristine PTB7, 80:20% PTB7:PCBM blend and 50:50% PTB7:PCBM blend. The films were prepared on PEDOT:PSS-coated Si substrates.

in-plane direction and a (010) reflection at  $1.62 \text{ \AA}^{-1}$  along the out-of-plane direction, indicating the presence of a crystalline PTB7 phase with a face-on orientation. The GIWAXS patterns of pristine PCBM showed scattering at  $1.37 \text{ \AA}^{-1}$  along the in-plane and out-of-plane directions simultaneously, indicating the presence of an aggregated PCBM phase without a preferred orientation.

The AFM height images of the 80:20% PTB7:PCBM blend were similar to those of pristine PTB7, with an estimated  $r_{\text{RMS}}$  of 0.62 nm, and showed an overall negative shift in the phase image as a result of well-dispersed PCBM (Fig. 2a, middle panel). The GIWAXS patterns of the 80:20% PTB7:PCBM blend were similar to those of pristine PTB7 but without additional scattering at  $1.37 \text{ \AA}^{-1}$  arising from an aggregated PCBM phase. In addition, the PL of the 80:20% PTB7:PCBM blend was quenched by  $\sim 99\%$  (Fig. S4). These results indicate that the added 20 wt% of PCBM was mainly dispersed in the PTB7 matrix in the 80:20% PTB7:PCBM blend, confirming the presence of a two-phase morphology composed of a crystalline PTB7 phase and a mixed phase (dispersed PCBM in amorphous PTB7 phase). In contrast, the 50:50% PTB7:PCBM blend exhibited rough surfaces (Fig. 2a, bottom panel) because of the presence of an

aggregated PCBM phase. The estimated  $r_{\text{RMS}}$  was 1.11 nm, which is approximately twice the  $r_{\text{RMS}}$  values of the pristine PTB7 and 80:20% PTB7:PCBM blend. The GIWAXS patterns of the 50:50% PTB7:PCBM blend showed clear scattering at  $1.37 \text{ \AA}^{-1}$  along both the in-plane and out-of-plane directions, indicating the presence of an aggregated PCBM phase. In particular, the 50:50% PTB7:PCBM blend showed overall negative phase images similar to those of the 80:20% PTB7:PCBM blend, indicating that the 50:50% PTB7:PCBM blend also contained well-dispersed PCBM. The almost complete PL quenching of the 50:50% PTB7:PCBM blend also supports the presence of well-dispersed PCBM in this blend. A detailed analysis of the PL quenching efficiencies of the blends is discussed in the Supporting Information (Fig. S4). These results confirm a three-phase morphology composed of crystalline PTB7 phase, aggregated PCBM phase, and a mixed phase for the 50:50% PTB7:PCBM blend. In addition, the cross-sectional SEM images of PTB7:PCBM blends demonstrate consistent morphological features out of the plane (perpendicular) (Fig. S5).

To compare the magnitudes of loss in the absorption and photooxidation of the blends, we used UV-Vis spectroscopy and FTIR spectroscopy (Figs. 3a and S6),

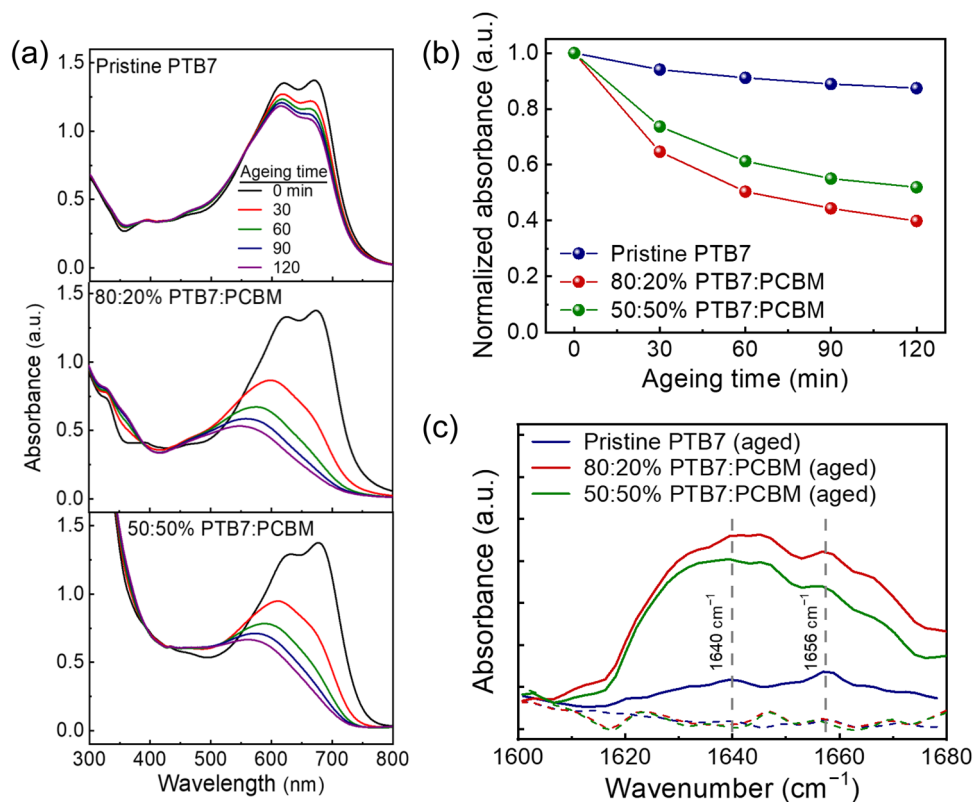


**Fig. 3** Spectroscopic analyses of the films during the aging process. Evolution of **a** UV-Vis absorption spectra, **b** normalized absorbance at 0–1 vibronic transition, and **c** FTIR spectra before (dashed lines) and after (solid lines) aging for 120 min of pristine PTB7, 80:20% PTB7:PCBM and 50:50% PTB7:PCBM blend under simulated AM 1.5 G illumination in dry air.

both of which are standard analytical tools for these purposes<sup>10–14</sup>. The pristine PTB7 tolerated aging relatively well, exhibiting a ~12% reduction in optical density in the 500–800 nm region after 120 min of aging. In addition, pristine PCBM showed almost unchanged absorption after 120 min of aging, indicating that PCBM has a higher photooxidative stability than pristine PTB7 (Fig. S7). However, the 80:20% PTB7:PCBM blend suffered severe loss in absorption: its optical density in the 500–800 nm region decreased by 60% after 120 min of aging, which is five times greater than the optical density loss of pristine PTB7 (Fig. 3b). These results show that a small fraction of PCBM can promote a substantial loss in the absorption of PTB7. Given the destabilization effect of PCBM, the loss in absorption of PTB7 should become increasingly severe with an increasing fraction of PCBM in the PTB7:PCBM blends. However, the 50:50% PTB7:PCBM blend showed a relatively smaller decrease in optical density (~50%) after 120 min of aging compared to the 80:20% PTB7:PCBM blend despite the additional 30 wt% of PCBM (Fig. 3b). Note that the pristine PTB7 and PTB7:PCBM blends exhibited similar losses in optical density under illumination in inert nitrogen, again confirming that the degradation was indeed driven by the combination of light and oxygen (Fig. S8).

In the FTIR spectra, the absorption peaks assigned to the C=C bonds ( $1568\text{ cm}^{-1}$ ) in the conjugated backbone and the alkyl groups ( $2850\text{--}2960\text{ cm}^{-1}$ ) in the side chains decrease with increasing aging time for all three blends, which is known to originate from the photooxidative structural destruction of PTB7<sup>36</sup>. Moreover, new absorption peaks emerge at 1300, 1490, 1656, and  $1640\text{ cm}^{-1}$  in the spectra of all three blends after 120 min of aging; however, the peaks in the spectrum of the 80:20% PTB7:PCBM blend are more intense than those in the spectra of the pristine PTB7 and the 50:50% PTB7:PCBM blend (Fig. 3c). According to the literature<sup>29</sup>, the absorption bands at 1300 and  $1656\text{ cm}^{-1}$  are consistent with the FTIR spectrum of 1,4-benzoquinone, and those at 1490 and  $1640\text{ cm}^{-1}$  correspond to the FTIR spectrum of 2-ethyl-1-hexene. Thus, these peaks indicate that photooxidative structural changes of PTB7 involve the cleavage of the ether groups on the benzodithiophene during aging. The increase in absorption in the 300–400 nm region for the aged 80:20% PTB7:PCBM blend is supportive evidence for the formation of 1,4-benzoquinone, which has an absorption profile near 300 nm<sup>37</sup>. Therefore, the 50:50% PTB7:PCBM blend exhibited enhanced photooxidative stability compared with the 80:20% PTB7:PCBM blend, similar to the trend observed in the UV–Vis spectra. These results indicate that the photooxidation of PTB7 is strongly dependent on the nanomorphology of PCBM, as indicated by the 50:50% PTB7:PCBM blend, which includes both dispersed PCBM

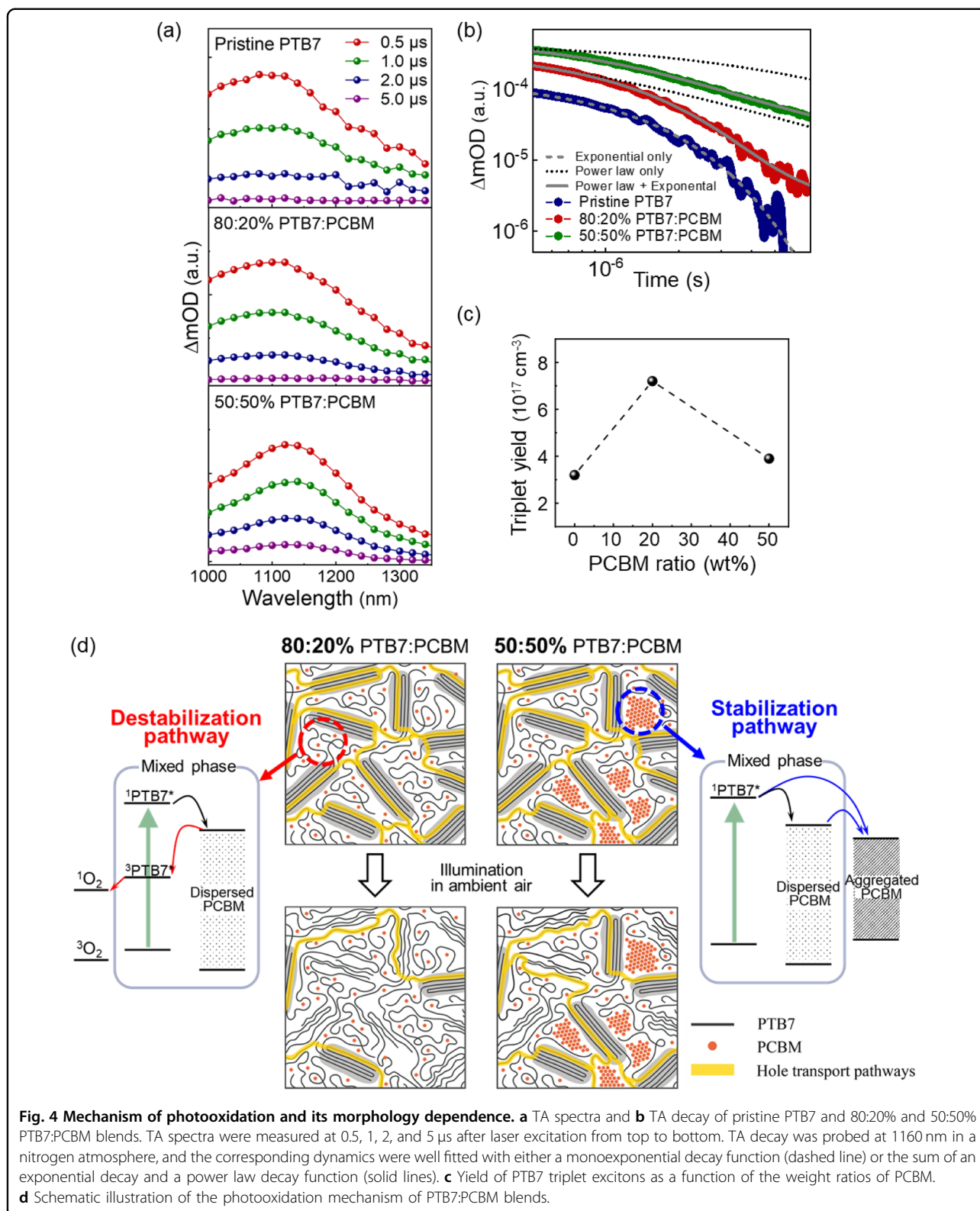
and aggregated PCBM, showing improved environmental stability compared with the 80:20% PTB7:PCBM blend, which includes mainly dispersed PCBM. That is, the destabilization effect of dispersed PCBM and the stabilization effect of aggregated PCBM coincide for the PTB7:PCBM blends, whose environmental stability is determined by the relative volume fractions of dispersed PCBM and aggregated PCBM.

### Photooxidation pathways facilitated by dispersed PCBM in PTB7:PCBM blends

To enable a detailed discussion of the photooxidation pathways in the PTB7:PCBM blends containing PCBM with different nanomorphologies, we collected the TA spectra of the pristine PTB7 and PTB7:PCBM blends. Figure 4a shows the TA spectra of the pristine PTB7 and PTB7:PCBM blends excited at a wavelength of 532 nm with a fluence of  $1.7\text{ }\mu\text{J cm}^{-2}$ . To avoid triplet–triplet annihilation, the excitation intensity was reduced using neutral-density filters. For the pristine PTB7 (Fig. 4a, top panel), a broad absorption band was observed from 1000 to 1360 nm with the maximum absorption at ~1100 nm. The decay dynamics were well fitted using a mono-exponential decay function with a lifetime of 1.1  $\mu\text{s}$  under a nitrogen atmosphere and 0.7  $\mu\text{s}$  under an oxygen atmosphere (Figs. 4b and S9). The accelerated lifetime under an oxygen atmosphere is characteristic of a triplet exciton, and this result is in good agreement with the results of a previous report<sup>12</sup>. We therefore assigned this positive absorption to a PTB7 triplet exciton.

Compared with the TA of pristine PTB7, that of the 50:50% PTB7:PCBM blend (Fig. 4a, bottom panel) shows a relatively narrow absorption band with a maximum absorption at ~1140 nm. The decay dynamics of optical density (OD) were well fitted by a combination of an exponential decay function and a power-law decay function with an exponent of  $\alpha$  (i.e.,  $\Delta\text{OD}(t) \propto t^{-\alpha}$ ), as shown in Fig. 4b. The power-law decay indicates the bimolecular recombination of dissociated charges in a matrix with energetic disorder<sup>10–12</sup>. This result indicates that the transient signal is attributable to two transient components: triplet excitons and polarons. For the 80:20% PTB7:PCBM blend (Fig. 4a, middle panel), little variation in TA was observed compared with that observed for pristine PTB7. The decay dynamics were also well fitted by the sum of an exponential decay function and a power-law decay function (Fig. 4b). However, the decay dynamics of the 80:20% PTB7:PCBM blend exhibited stronger exponential decay dynamics than that of the 50:50% PTB7:PCBM blend, indicating that the transient signal is attributable mainly to triplet excitons.

In principle, triplet excitons can form by three pathways: (1) the bimolecular recombination of dissociated polarons<sup>38</sup>, (2) intersystem crossing (ISC) from the singlet



excited states of polymers<sup>12</sup>, and (3) singlet fission under very high excitation intensity<sup>39</sup>. In the measurements, the PL was almost completely quenched for the 80:20% and

50:50% PTB7:PCBM blends (Fig. S4); thus, singlet excitons should have been quenched before ISC occurred considering the much slower timescale of the ISC process.

In addition, a singlet fission pathway can be excluded because the blends were excited under a very weak excitation fluence. Therefore, the formation of triplet excitons in the blends can be conjectured to originate predominantly from the bimolecular recombination of dissociated polarons. Consequently, triplet excitons can be generated in all the films even though their yield varied as a function of the weight fraction of PCBM.

We next examined how the variation in the yield of triplet excitons affected the photooxidation of PTB7 according to the nanomorphologies of PCBM within the PTB7:PCBM blends. As previously mentioned, the transient signal on a time scale of microseconds was fitted with a monoexponential decay function for the pristine PTB7 and with the sum of an exponential decay and a power-law decay for the 80:20% and 50:50% PTB7:PCBM blends (Table S3). Among the fitting parameters, the preexponential factor was used to calculate the density of triplet excitons. That is, the  $\Delta OD(t)$  of the transient signals was converted into the density of triplet excitons,  $N(t)$ , according to the Beer–Lambert law:  $N(t) = \Delta OD(t) N_A (1000\epsilon L)^{-1}$ , where  $N_A$  is Avogadro's constant,  $\epsilon$  is the molar absorption coefficient, and  $L$  is the film thickness. The  $\epsilon$  value of another conjugated polymer ( $\epsilon = 8.7 \times 10^3 \text{ M}^{-1} \text{ cm}^{-1}$ ) with a backbone similar to that of PTB7 was used<sup>39</sup>, assuming that the  $\epsilon$  values of the triplet excitons of the two polymers are not substantially different from each other. The density of triplet excitons was larger in the PTB7:PCBM blends than in pristine PTB7 (Fig. 4c and Table S3), suggesting that the formation yield of triplet excitons resulting from the bimolecular recombination of the PTB7:PCBM blends overwhelmed the yield generated by the direct ISC from the singlet states of pristine PTB7. Interestingly, the density of triplet excitons in the PTB7:PCBM blends was influenced by the nanomorphology of the PCBM. The photoexcitation of the 80:20% PTB7:PCBM blend yielded a higher density of triplet excitons than the photoexcitation of the 50:50% PTB7:PCBM blend. These results indicate that dispersed PCBM accelerated the formation of PTB7 triplet excitons, whereas the presence of aggregated PCBM lessened the formation of PTB7 triplet excitons.

Other authors have reported that electron delocalization by fullerene aggregation effectively reduces the formation of triplet excitons of a polymer donor<sup>38</sup>. The spin-triplet charge-transfer (CT) states generated by the bimolecular recombination of free charges can either relax to form polymer triplet excitons or redissociate into free charges (Fig. S10)<sup>40</sup>; as the CT state became increasingly delocalized, the relaxation to a polymer triplet was suppressed because of the facilitated redissociation of the CT states into free charges<sup>38</sup>. The higher density of triplet excitons in the 80:20% PTB7:PCBM blend than in the 50:50% PTB7:PCBM blend in our results

can be reasonably explained in the same context. That is, in the 80:20% blend, PCBM is dispersed rather than aggregated; the CT states generated by bimolecular recombination should therefore be relatively more localized compared with those generated in the 50:50% blend. This difference would reduce the redissociation of the CT states into free charges and increase the generation of triplet excitons, resulting in lower  $J_{SC}$ , FF, and PCE values for the 80:20% PTB7:PCBM OSC devices than for the 50:50% PTB7:PCBM OSC devices (Tables S1 and S4).

We then focused on the mechanism of photooxidation of the blends. In OSCs, photooxidation by singlet oxygen has been widely reported<sup>12</sup>. In general, photooxidation by singlet oxygen requires the formation of triplet excitons with lifetimes longer than several hundreds of nanoseconds and an energy level of triplet states suitable for generating singlet oxygen<sup>12</sup>. As we previously mentioned, the former condition was satisfied for all the blends. To confirm the latter condition, we evaluated the energy level of the singlet state of PTB7 from the intersection point of the normalized absorption and emission spectra (Fig. S11)<sup>41</sup>. The energy level was estimated to be  $\sim 1.7$  eV; consequently, the triplet state of PTB7 was estimated to be slightly above 1.0 eV on the basis of empirical relationships with conjugated polymers, in which the triplet state lies  $\sim 0.6$ – $0.7$  eV below the singlet state<sup>42</sup>. This triplet energy level above 1.0 eV implies that the formation of singlet oxygen (0.98 eV)<sup>12</sup> from the triplet states of PTB7 was energetically favorable. Our experimental results show good agreement between the degree of photooxidation and the yield of PTB7 triplet excitons, strongly supporting our hypothesis that the generation of triplet-mediated singlet oxygen is the main cause of the photooxidation of the PTB7:PCBM blend.

From the above results, the effects of the nanomorphologies of PCBM on the photooxidation of the PTB7:PCBM blends can be summarized as illustrated in Fig. 4d (see also Fig. S10). The photooxidation of the pristine and blend films is mainly caused by the singlet oxygen produced by the energy transfer from the triplet excitons of PTB7 to oxygen molecules. The yield of PTB7 triplet excitons is larger in the PTB7:PCBM blends than in the pristine PTB7 because the existence of PCBM in the blends leads to the formation of large amounts of triplet excitons by the bimolecular recombination of free charge carriers (denoted as the “destabilization pathway” in Fig. 4d), while only a small amount of triplet excitons can be formed in the pristine film by ISC. Among the blends, the triplet yield is larger in the 80:20% PTB7:PCBM blend than in the 50:50% PTB7:PCBM blend. This is because in the 50:50% blend, the destabilization pathway is partially suppressed by the aggregated PCBM phase, which reduces the formation of triplet excitons by the delocalization of electrons in the aggregated phase (denoted as the

“stabilization pathway” in Fig. 4d). Therefore, the degree of photooxidation was most severe in the 80:20% blend, followed by the 50:50% blend and pristine PTB7.

### Significant deterioration of hole transport in PTB7:PCBM blends by photooxidized PTB7

The accelerated photooxidation of PTB7 by dispersed PCBM led to a 50–60% loss in absorption in the PTB7:PCBM blends after 120 min of aging (Fig. 3b). However, the efficiency loss in the PTB7:PCBM OSC devices is two orders of magnitude (Fig. 1b and Table S1); thus, the loss in absorption alone cannot account for the loss of efficiency. Factors other than the loss in absorption, such as the degradation of electronic properties, likely contributed to the efficiency loss in the PTB7:PCBM OSC devices. As previously mentioned, the photooxidation of PTB7 is associated with an alteration of the chemical structure; we therefore speculated that the photooxidation of PTB7 would also affect the hole transport properties of the PTB7:PCBM blends.

The deterioration of hole transport by photooxidation could be observed indirectly by collecting the photocurrent density ( $J_{ph}$ ) vs. effective voltage ( $V_{eff}$ ) curves and EQE spectra of the fresh and aged PTB7:PCBM OSC devices. The  $J_{ph}$  vs.  $V_{eff}$  curves document a steady collection of dissociated charge carriers by electrodes with increasing  $V_{eff}$ , where  $J_{ph}$  generally reaches saturation ( $J_{sat}$ ) at high  $V_{eff}$ . The fresh PTB7:PCBM OSC devices showed a  $J_{sat}$  at a high  $V_{eff}$  of 1 V (Fig. S12), indicating that all of the dissociated charge carriers were efficiently collected by the electrodes at a high  $V_{eff}$ . For all the aged PTB7:PCBM OSC devices, however,  $J_{ph}$  gradually increased without  $J_{sat}$  as  $V_{eff}$  increased, indicating that they exhibited poor charge collection. In addition, the highest value in the EQE spectra decreased by 98% after 120 min of aging, which represents a >50% loss in optical density, indicating that free charge carriers could not reach the electrode (Figs. 1c and 3b). This trend possibly implies the deterioration of hole transport by oxidized PTB7 in the PTB7:PCBM OSC devices.

Inspired by these results, we quantified the deterioration of hole transport in PTB7:PCBM blends under illumination in dry air, where the blends contained PCBM with different nanomorphologies. Symmetric hole-only devices with structures of ITO/PEDOT:PSS/PTB7:PCBM/MoO<sub>3</sub>/Al (ITO = indium tin oxide) were fabricated for this purpose. The space-charge-limited currents (SCLCs) of the devices were characterized by the Mott–Gurney square law:

$$J = \frac{9}{8} \epsilon_0 \epsilon_r \mu \frac{V^2}{L^3} \quad (1)$$

where  $J$  is the current density,  $\epsilon_0$  is the permittivity of free space,  $\epsilon_r$  is the dielectric constant of the films,  $\mu$  is the charge carrier (hole) mobility,  $V$  is the applied voltage, and

$L$  is the layer thickness<sup>43</sup>. To validate the fabrication of ideal hole-only devices with Ohmic contacts, we verified that the measured hole currents were space-charge limited. As established in Eq. (1), two prerequisites for satisfying the criterion for SCLCs are a quadratic voltage dependence and an  $L^{-3}$  layer-thickness dependence. The layer-thickness dependence can be directly confirmed by plotting  $JL^3$  as a function of  $V$ , whereby  $JL^3-V$  curves coalesce onto a single curve if the SCLC prerequisites are indeed satisfied. The measured hole currents of all the tested PTB7:PCBM blends showed quadratic voltage dependence at high  $V$  and layer-thickness dependence (Fig. S13), demonstrating that the measured hole currents were indeed space-charge limited. These results demonstrate that ideal hole-only devices based on PTB7:PCBM blends with different PCBM morphologies were attained, enabling a comparison of the hole transport in fresh and aged PTB7:PCBM blends.

Figure 5a–d shows the evolution of hole currents in PTB7:PCBM blends with different fractions of PCBM having undergone different aging times under illumination in dry air prior to top electrode deposition. Hole mobilities ( $\mu_h$ ) were derived by fitting the hole current density with the Mott–Gurney square law. Surprisingly, oxidized PTB7 caused substantial deterioration of the hole transport properties. The hole currents of the 80:20% PTB7:PCBM blend, which exhibited severe photooxidation, decreased substantially. Its hole mobility decreased by four orders of magnitude after 120 min of aging, representing a >60% loss of optical density (Fig. 5b). Even pristine PTB7, which showed a 10% loss of optical density, exhibited an order-of-magnitude decrease in mobility after 120 min of aging (Fig. 5a). In particular, the 50:50% PTB7:PCBM blend, which was partially stabilized by the aggregated PCBM phase, exhibited a hole mobility decreased by two orders of magnitude after 120 min of aging, which is comparable to the efficiency losses in the PTB7:PCBM OSC devices (Fig. 5c). These results show a strong correlation between the degradation of hole transport by oxidized PTB7 and the loss of efficiency in OSC devices.

We next sought to determine how oxidized PTB7 degrades the hole transport properties of the PTB7:PCBM blends. The evolution of the volume and nanoscale packing of the crystalline PTB7 phases in the pristine PTB7 and blends during aging was investigated by using GIWAXS (Fig. 5e, with detailed parameters in Table S5). For all the PTB7:PCBM blends, the volume of the crystalline PTB7 phase decreased, and its  $\pi$ – $\pi$  stacking distance increased after aging. In particular, the 80:20% PTB7:PCBM blend, which showed severe photooxidation, underwent substantial morphological degradation during aging compared with the pristine PTB7 and 50:50% PTB7:PCBM blend. The intensity of its (100) reflection decreased by 40% after aging, indicating a loss of the

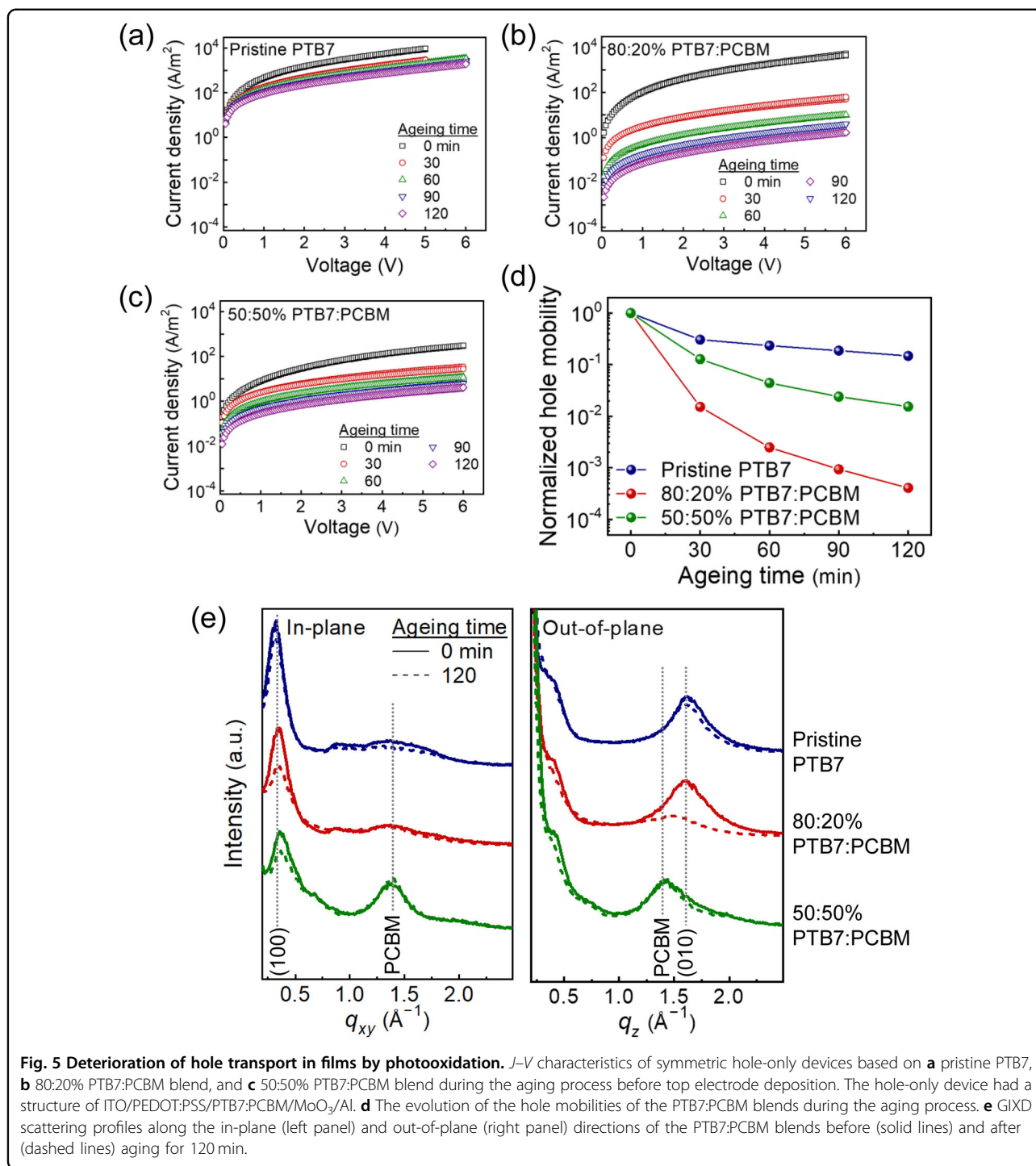
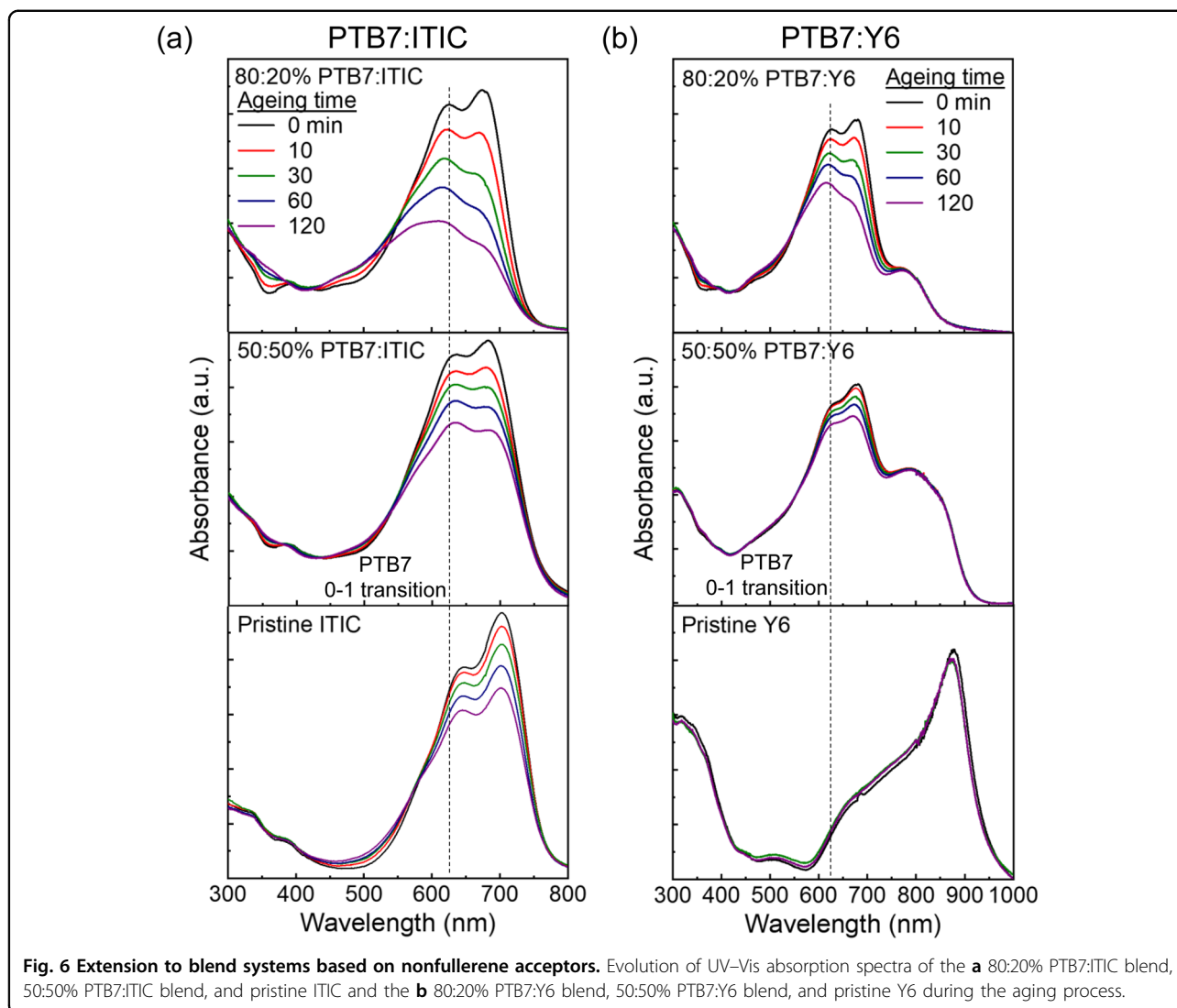


**Fig. 5** Deterioration of hole transport in films by photooxidation.  $J-V$  characteristics of symmetric hole-only devices based on **a** pristine PTB7, **b** 80:20% PTB7:PCBM blend, and **c** 50:50% PTB7:PCBM blend during the aging process before top electrode deposition. The hole-only device had a structure of ITO/PEDOT:PSS/PTB7:PCBM/MoO<sub>3</sub>/Al. **d** The evolution of the hole mobilities of the PTB7:PCBM blends during the aging process. **e** GIXD scattering profiles along the in-plane (left panel) and out-of-plane (right panel) directions of the PTB7:PCBM blends before (solid lines) and after (dashed lines) aging for 120 min.

lamellar structural order of the side chains due to the photooxidation-induced side-chain cleavage of PTB7. In addition, the intensity of its (010) reflection substantially decreased by 60% after aging, indicating reduced  $\pi$ - $\pi$  stacking of the backbone moieties, possibly because side-chain cleavage increases the conformational diversity of the PTB7 backbone. The  $\pi$ - $\pi$  stacking distance of this

blend, as extracted from its (010) reflection in the GIWAXS pattern, increased from 3.90 to 4.22 nm after aging, which is unfavorable for the hopping transport of holes. The evolution of the GIWAXS patterns of the pristine PTB7 and the 50:50% PTB7:PCBM blend showed similar trends, with relatively small variance compared with the evolution of the GIWAXS patterns of the 80:20%



PTB7:PCBM blend. These GIWAXS results are strongly correlated with the UV-Vis results of the PTB7:PCBM blends (Fig. 3a). The evolution of the 0-0 to 0-1 vibronic peak ratio, which indicates the degree of crystallinity<sup>44</sup>, gradually decreased with increasing aging time, correlating with a gradual blueshift of the overall absorption spectrum. These results indicate that a structural change in PTB7 caused by photooxidation substantially disrupts the long-range structural order of the crystalline PTB7 phases. This change decreases the volumes of the crystalline PTB7 phases, thereby decreasing the number of hole transport pathways within the PTB7:PCBM blends, resulting in poor hole transport<sup>45–48</sup>.

#### Extension to blend systems based on nonfullerene acceptors

To investigate the generality of this phenomenon, we extended our studies to other blends comprising

benchmark nonfullerene acceptors: ITIC (Figs. 6a and S14) and Y6 (Figs. 6b and S16). The PTB7:ITIC blends and PTB7:Y6 blends showed environmental instabilities at 80:20% ratios but enhanced environmental stabilities at 50:50% ratios (Figs. S15 and S17), demonstrating a phenomenon qualitatively similar to the responses of the PTB7:PCBM blends. Therefore, the destabilization/stabilization pathways caused by dispersed/aggregated acceptors could be applied to other blend systems.

The observations presented herein suggest that minimizing the formation of triplet excitons via bimolecular recombination by dispersed acceptors could be a fundamental approach for enhancing the environmental stability of OSC devices. According to previous studies<sup>49</sup>, separated electrons in a dispersed acceptor can transfer to an aggregated acceptor phase with lower-energy sites. However, a dispersed acceptor isolated from an aggregated acceptor phase will cause the formation of triplet

excitons, resulting in triplet-mediated singlet oxygen generation and the photooxidation of polymer: small-molecule blends. Therefore, to enhance the environmental stability of OSC devices, the amount of dispersed acceptor isolated from the aggregated acceptor phase must be minimized. Our results are also likely to aid in understanding the environmental stability of other electronic devices that use a blend of organic semiconductors, such as organic light-emitting diodes and organic photodetectors.

## Conclusions

The effects of small-molecule acceptors on the environmental stability of polymer: small-molecule blends have been controversial because of contradictory results supporting both a stabilization and a destabilization effect of small-molecule acceptors. Our work demonstrates that these contradictory results are consequences of the contradictory effects of the nanomorphologies of small-molecule acceptors, i.e., dispersed acceptors and aggregated acceptors. In the case of polymer:fullerene blends, PTB7:PCBM, a blend that contains mostly dispersed PCBM, undergoes severe photooxidation under illumination in dry air, whereas a blend containing both dispersed PCBM and aggregated PCBM exhibits a relatively enhanced environmental stability compared with a blend composed mainly of dispersed PCBM. The dispersed PCBM accelerates the formation of PTB7 triplet excitons by bimolecular recombination, resulting in the generation of singlet oxygen and, hence, the severe photooxidation of PTB7. In contrast, the aggregated PCBM alleviates the formation of PTB7 triplet excitons through delocalized CT states, leading to the stabilization of PTB7. We also investigated the effect of oxidized PTB7 on the hole transport properties of PTB7:PCBM blends to explain the substantial efficiency losses of the PTB7:PCBM OSC devices. For all of the investigated PTB7:PCBM blends, aging resulted in more severe degradation of hole transport than the loss of light absorption, which exhibited a strong correlation with the efficiency losses in the PTB7:PCBM OSC devices. The deterioration of hole transport is mainly driven by the loss of the crystalline PTB7 phase due to photooxidation of the PTB7 chains, resulting in diminished hole transport pathways within the films. We extended our conclusions to the polymer:nonfullerene blends PTB7:ITIC and PTB7:Y6, thereby confirming the generality of this phenomenon in polymer:small-molecule organic solar cells.

## Acknowledgements

This work was supported by the National Research Foundation of Korea (NRF) grant (2020R1A2C3004477, 2021R1A4A1030944) funded by the Ministry of Science and ICT, Korea. This work was also supported by the Basic Science Research Program through NRF funded by the Ministry of Education (2020R1A6A3A03040410). The authors thank the Pohang Accelerator

Laboratory for providing the synchrotron radiation sources at the 9A, 3C, and 5A beamlines used in this study.

## Author details

<sup>1</sup>Department of Chemical Engineering, Pohang University of Science and Technology (POSTECH), Pohang 37673, Republic of Korea. <sup>2</sup>Department of Chemical and Biological Engineering, Gachon University, Seongnam 13120, Republic of Korea. <sup>3</sup>Department of Nanotechnology and Advanced Materials Engineering, Sejong University, Seoul 05006, Republic of Korea. <sup>4</sup>Department of Polymer Chemistry and Graduate School of Engineering, Kyoto University, Katsura, Nishikyo-ku, Kyoto 615-8510, Japan

## Author contributions

W.S. and H.L. contributed equally to this work. W.S., H.L., W.C., H.D.K., and K.C. conceived the concept and designed the experiment. W.S., H.L., and H.D.K. predominantly carried out the device experiments. W.C., S.G.H., J.K., K.C., and S.H.K. assisted in carrying out the device experiments. W.S., H.L., D.L., H.D.K., H.O., and K.C. analyzed the results. W.S., H.L., H.D.K., and K.C. wrote and revised the manuscript. All authors discussed the results and commented on the manuscript.

## Conflict of interest

The authors declare no competing interests.

## Publisher's note

Springer Nature remains neutral with regard to jurisdictional claims in published maps and institutional affiliations.

**Supplementary information** The online version contains supplementary material available at <https://doi.org/10.1038/s41427-022-00400-9>.

Received: 7 December 2021 Revised: 29 April 2022 Accepted: 9 May 2022.  
Published online: 8 July 2022

## References

- Liu, Q. et al. 18% efficiency organic solar cells. *Sci. Bull.* **65**, 272–275 (2020).
- Zhang, M. et al. Single-layered organic photovoltaics with double cascading charge transport pathways: 18% efficiencies. *Nat. Commun.* **12**, 309 (2021).
- Ye, L. et al. Quantitative relations between interaction parameter, miscibility and function in organic solar cells. *Nat. Mater.* **17**, 253–260 (2018).
- Lee, H., Park, C., Sin, D. H., Park, J. H. & Cho, K. Recent advances in morphology optimization for organic photovoltaics. *Adv. Mater.* **30**, 1800453 (2018).
- Kim, M. et al. Critical factors governing vertical phase separation in polymer–PCBM blend films for organic solar cells. *J. Mater. Chem. A* **4**, 15522–15535 (2016).
- Lee, H. et al. Effect of donor–acceptor molecular orientation on charge photogeneration in organic solar cells. *NPG Asia Mater.* **10**, 469–481 (2018).
- Lee, J. et al. Design of nonfullerene acceptors with near-infrared light absorption capabilities. *Adv. Energy Mater.* **8**, 1801209 (2018).
- Xiao, S., Zhang, Q. & You, W. Molecular engineering of conjugated polymers for solar cells: an updated report. *Adv. Mater.* **29**, 1601391 (2017).
- Pelzer, K. M. & Darling, S. B. Charge generation in organic photovoltaics: a review of theory and computation. *Mol. Syst. Des. Eng.* **1**, 10–24 (2016).
- Soon, Y. W. et al. Material crystallinity as a determinant of triplet dynamics and oxygen quenching in donor polymers for organic photovoltaic devices. *Adv. Funct. Mater.* **24**, 1474–1482 (2014).
- Mateker, W. R. et al. Molecular packing and arrangement govern the photooxidative stability of organic photovoltaic materials. *Chem. Mater.* **27**, 6345–6353 (2015).
- Soon, Y. W. et al. Correlating triplet yield, singlet oxygen generation and photochemical stability in polymer/fullerene blend films. *Chem. Commun.* **49**, 1291–1293 (2013).
- Hoke, E. T. et al. The role of electron affinity in determining whether fullerenes catalyze or inhibit photooxidation of polymers for solar cells. *Adv. Energy Mater.* **2**, 1351–1357 (2012).
- Speller, E. M. et al. Toward improved environmental stability of polymer: fullerene and polymer:nonfullerene organic solar cells: A common energetic origin of light- and oxygen-induced degradation. *ACS Energy Lett.* **4**, 846–852 (2019).

15. Jørgensen, M., Norrman, K. & Krebs, F. C. Stability/degradation of polymer solar cells. *Sol. Energy Mater. Sol. Cells* **92**, 686–714 (2008).
16. Lee, H. et al. Enhanced organic solar cell stability through the effective blocking of oxygen diffusion using a self-passivating metal electrode. *ChemSusChem* **9**, 445–454 (2016).
17. Newman, M. J. et al. Photo-stability study of a solution-processed small molecule solar cell system: Correlation between molecular conformation and degradation. *Sci. Technol. Adv. Mater.* **19**, 194–202 (2018).
18. Luke, J. et al. Twist and degrade—impact of molecular structure on the photostability of nonfullerene acceptors and their photovoltaic blends. *Adv. Energy Mater.* **9**, 1803755 (2019).
19. Distler, A. et al. Effect of PCBM on the photodegradation kinetics of polymers for organic photovoltaics. *Chem. Mater.* **24**, 4397–4405 (2012).
20. Bartesaghi, D., Ye, G., Chiechi, R. C. & Koster, L. J. A. Compatibility of PTB7 and [70]PCBM as a key factor for the stability of PTB7:[70]PCBM solar cells. *Adv. Energy Mater.* **6**, 1502338 (2016).
21. Neugebauer, H., Brabec, C., Hummelen, J. C. & Sariciftci, N. S. Stability and photodegradation mechanisms of conjugated polymer/fullerene plastic solar cells. *Sol. Energy Mater. Sol. Cells* **61**, 35–42 (2000).
22. Chambon, S., Rivaton, A., Gardette, J.-L. & Firon, M. Photo- and thermal degradation of MDMO-PPV:PCBM blends. *Sol. Energy Mater. Sol. Cells* **91**, 394–398 (2007).
23. Reese, M. O. et al. Photoinduced degradation of polymer and polymer-fullerene active layers: experiment and theory. *Adv. Funct. Mater.* **20**, 3476–3483 (2010).
24. Razzell-Hollis, J. et al. Photochemical stability of high efficiency PTB7:PC<sub>70</sub>BM solar cell blends. *J. Mater. Chem. A* **2**, 20189–20195 (2014).
25. Speller, E. M. et al. Impact of aggregation on the photochemistry of fullerene films: correlating stability to triplet exciton kinetics. *ACS Appl. Mater. Interfaces* **9**, 22739–22747 (2017).
26. Chambon, S., Rivaton, A., Gardette, J.-L. & Firon, M. Reactive intermediates in the initiation step of the photo-oxidation of mdmo-ppv. *J. Polym. Sci. A Polym. Chem.* **47**, 6044–6052 (2009).
27. Sai, N., Leung, K., Zador, J. & Henkelman, G. First principles study of photo-oxidation degradation mechanisms in P3HT for organic solar cells. *Phys. Chem. Chem. Phys.* **16**, 8092–8099 (2014).
28. Tournebise, A. et al. Impact of UV-visible light on the morphological and photochemical behavior of a low-bandgap poly(2,7-carbazole) derivative for use in high-performance solar cells. *Adv. Energy Mater.* **3**, 478–487 (2013).
29. Savikhin, V. et al. Morphological, chemical, and electronic changes of the conjugated polymer ptb7 with thermal annealing. *iScience* **2**, 182–192 (2018).
30. González, D. M. et al. Codependence between crystalline and photovoltage evolutions in P3HT:PCBM solar cells probed with in-Operando GIWAXS. *ACS Appl. Mater. Interfaces* **9**, 3282–3287 (2017).
31. Liu, F. et al. Understanding the morphology of PTB7:PCBM blends in organic photovoltaics. *Adv. Energy Mater.* **4**, 1301377 (2014).
32. Schaffer, C. J. et al. A direct evidence of morphological degradation on a nanometer scale in polymer solar cells. *Adv. Mater.* **25**, 6760–6764 (2013).
33. Schaffer, C. J. et al. Morphological degradation in low bandgap polymer solar cells – an in operando study. *Adv. Energy Mater.* **6**, 1600712 (2016).
34. Yang, D. et al. In operando GISAXS and GIWAXS stability study of organic solar cells based on PffBT4T-2OD:PC<sub>71</sub>BM with and without solvent additive. *Adv. Sci.* **7**, 2001117 (2020).
35. Wienhold, K. S. et al. Following in operando the structure evolution-induced degradation in printed organic solar cells with nonfullerene small molecule acceptor. *Sol. RRL* **4**, 2000251 (2020).
36. Löhner, F. C. et al. Light-induced and oxygen-mediated degradation processes in photoactive layers based on PTB7-Th. *Adv. Photon. Res.* **1**, 2000047 (2020).
37. Wilke, T., Schneider, M. & Kleinermanns, K. 1,4-Hydroquinone is a hydrogen reservoir for fuel cells and recyclable via photocatalytic water splitting. *Open J. Phys. Chem.* **03**, 97–102 (2013).
38. Rao, A. et al. The role of spin in the kinetic control of recombination in organic photovoltaics. *Nature* **500**, 435–439 (2013).
39. Busby, E. et al. A design strategy for intramolecular singlet fission mediated by charge-transfer states in donor-acceptor organic materials. *Nat. Mater.* **14**, 426–433 (2015).
40. Gillett, A. J. et al. The role of charge recombination to triplet excitons in organic solar cells. *Nature* **597**, 666–671 (2021).
41. Vandewal, K., Benduhn, J. & Nikolis, V. C. How to determine optical gaps and voltage losses in organic photovoltaic materials. *Sustain. Energy Fuels* **2**, 538–544 (2018).
42. Freeman, D. M. E. et al. Synthesis and exciton dynamics of donor-orthogonal acceptor conjugated polymers: Reducing the singlet-triplet energy gap. *J. Am. Chem. Soc.* **139**, 11073–11080 (2017).
43. Mark, P. & Helfrich, W. Space-charge-limited currents in organic crystals. *J. Appl. Phys.* **33**, 205–215 (1962).
44. Spano, F. C. & Silva, C. H- and J-aggregate behavior in polymeric semi-conductors. *Annu. Rev. Phys. Chem.* **65**, 477–500 (2014).
45. Chabinyc, M. L., Toney, M. F., Kline, R. J., McCulloch, I. & Heeney, M. X-ray scattering study of thin films of poly(2,5-bis(3-alkylthiophen-2-yl)thieno[3,2-b]thiophene). *J. Am. Chem. Soc.* **129**, 3226–3237 (2007).
46. Lee, J. et al. Highly crystalline low-bandgap polymer nanowires towards high-performance thick-film organic solar cells exceeding 10% power conversion efficiency. *Energy Environ. Sci.* **10**, 247–257 (2017).
47. Jo, S. B. et al. Boosting photon harvesting in organic solar cells with highly oriented molecular crystals via graphene organic heterointerface. *ACS Nano* **9**, 8206–8219 (2015).
48. Kang, B. et al. Side-chain-induced rigid backbone organization of polymer semiconductors through semifluoroalkyl side chains. *J. Am. Chem. Soc.* **138**, 3679–3686 (2016).
49. Buchaca-Domingo, E. et al. Additive-assisted supramolecular manipulation of polymer:fullerene blend phase morphologies and its influence on photo-physical processes. *Mater. Horiz.* **1**, 270–279 (2014).